ACSNANO www.acsnano.org

ARTICLE

Hierarchical Organization of Organic Dyes and Protein Cages into Photoactive Crystals

Joona Mikkilä,[†] Eduardo Anaya-Plaza,[‡] Ville Liljeström,[†] Jose R. Caston,[§] Tomas Torres,*[,‡] Andrés de la Escosura,*[,‡] and Mauri A. Kostiainen*[,†]

[†]Biohybrid Materials, Department of Biotechnology and Chemical Technology, Aalto University, FI-00076 Aalto, Finland
[‡]Departamento de Química Orgánica, Universidad Autónoma de Madrid/IMDEA Nanociencia (TT), 28049 Madrid, Spain
[§]Department of Structure of Macromolecules, Centro Nacional de Biotecnología/CSIC, Cantoblanco, 28049 Madrid, Spain

Supporting Information

ABSTRACT: **Phthalocyanines (Pc) are non-natural organic dyes with wide and deep impact in materials science, based on their intense absorption at the near-infrared (NIR), long-lived fluorescence and high singlet oxygen ($^1O_2$) quantum yields. However, Pcs tend to stack in buffer solutions, losing their ability to generate singlet oxygen, which limits their scope of application. Furthermore, Pcs are challenging to organize in crystalline structures. Protein cages, on the other hand, are very promising biological building blocks that can be used to organize different materials into crystalline nanostructures. Here, we combine both kinds of components into photoactive biohybrid crystals. Toward this end, a hierarchical organization process has been designed in which (a) a supramolecular complex is formed between octacationic zinc Pc (1) and a tetraanionic pyrene (2) derivatives, driven by electrostatic and $\pi-\pi$ interactions, and (b) the resulting tetracationic complex acts as a molecular glue that binds to the outer surface anionic patches of the apoferritin (aFt) protein cage, inducing cocrystallization. The obtained ternary face-centered cubic (fcc) packed cocrystals, with diameters up to 100 μm, retain the optical properties of the pristine dye molecules, such as fluorescence at 695 nm and efficient light-induced $^1O_2$ production. Considering that $^1O_2$ is utilized in important technologies such as photodynamic therapy (PDT), water treatments, diagnostic arrays and as an oxidant in organic synthesis, our results demonstrate a powerful methodology to create functional biohybrid systems with unprecedented long-range order. This approach should greatly aid the development of nanotechnology and biomedicine.**

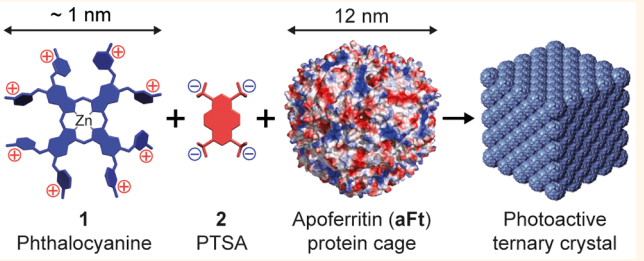

KEYWORDS: *singlet oxygen, phthalocyanine, ferritin, protein cage, self-assembly, crystal*

Creating functional, biocompatible and stimuli-responsive crystalline arrays from nanoscale building blocks is a field of growing interest, and aims to develop new biomedical and nanotechnology applications based on bottom-up and self-templating techniques.[1−6] For example, complexes with catalytic,[7,8] electronic,[9] magnetic,[10] optical[2,11,12] and plasmonic[13] properties have been presented during recent years. Furthermore, creating binary[14] and ternary[15] self-assemblies enable combining several functionalities into the same nanostructure. As a driving force for self-assembly, DNA base pairing[8,16] and alkanethiolate-stabilization[13] have for example been utilized. Higher-order structures can also be self-assembled through electrostatic interactions between biomacromolecules[17,18] or dendrimers and protein cages.[19−21]

Protein cages, such as virus capsids and apoferritin (**aFt**),[22] are particularly interesting biological building blocks to be organized into higher-order superlattices, because their inner cavity can be loaded with a variety of organic and inorganic materials.[23−26] However, crystalline coassemblies of protein cages and functional synthetic components are rare.[17,19,20] Moreover, the development of photoactive biohybrid crystals is a highly desirable, unmet goal within the field. Toward this end, herein we present the first organic dye/protein cage crystalline structure, composed of a tetracationic (1:1) complex between the zinc phthalocyanine (ZnPc, **1**)[27] and 1,3,6,8-pyrenetetrasulfonic acid (PTSA, **2**), which act as a molecular glue that can be further crystallized together with **aFt**[28] (pI ∼ 4.5) (Figure 1). This hierarchical self-assembly process, driven by electrostatic interactions with the exterior negatively charged patches of the **aFt** cage, results in optically active and robust ternary face-centered cubic (fcc) packed crystals with diameters up to 100 μm. Importantly, the **1**−**2**−**aFt** crystals are able to produce singlet oxygen upon irradiation. Furthermore, they can be disassembled by increasing the electrolyte concentration of the

Received: November 13, 2015
Accepted: December 21, 2015
Published: December 21, 2015

   DOI: 10.1021/acsnano.5b07167
ACS Nano 2016, 10, 1565−1571

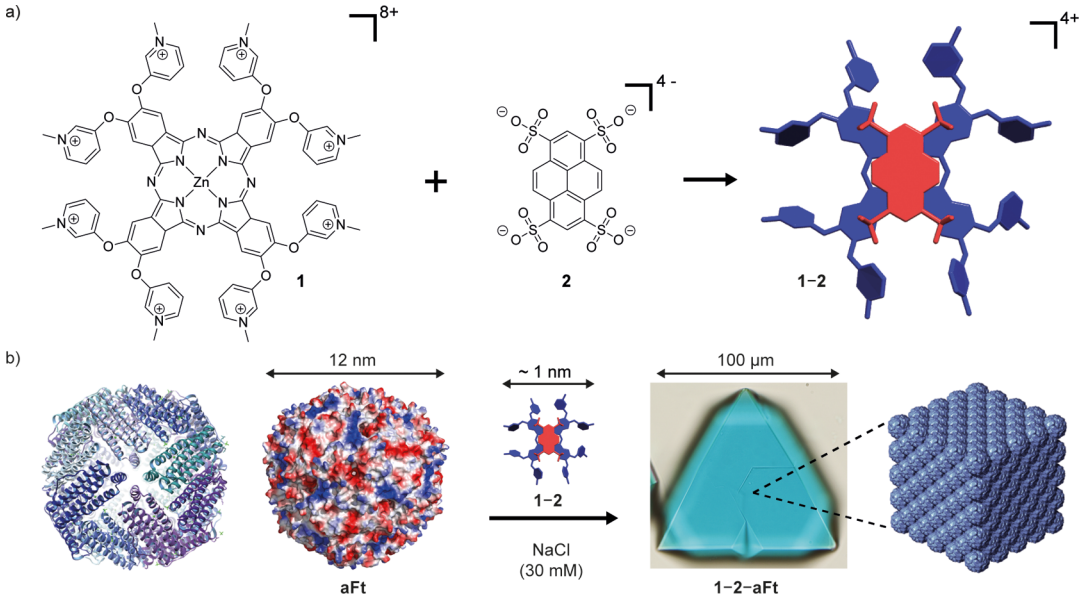

Figure 1. Scheme of the followed hierarchical strategy toward photoactive biohybrid crystals (1−2−aFt). (a) Chemical structures of 1 and 2, where sulfate and sodium are the respective counterions and the self-assembly of tetracationic 1−2 supramolecular complex. (b) Illustrations of the 12 nm sized aFt cage and its further cocrystallization with 1−2 complex driven by electrostatic interactions. Illustrations of aFt show the folded protein subunits (left) and the calculated electrostatic surface potential (right) with negatively charged patches (in red) covering the cage surface. Note that the cartoons of 1−2, aFt and the crystals are not in the same scale.

surrounding solution, representing the first case of a stimuli-responsive photosensitizing crystalline phase.

Optical activity in the presented biohybrid crystals relies on the phthalocyanine (Pc) component. Pc are non-natural organic dye photosensitizers (PS) with wide and deep impact in materials science.[29,30] Because of their extended conjugation, Pc absorb intensely at the near-infrared (NIR) spectral region (*ca.* 650−700 nm). The energy of the resulting excited state can be utilized for different optoelectronic and biomedical technologies.[31−33] In particular, Pc are well-known for their ability to generate singlet oxygen ($^1O_2$), a highly reactive species with prominent use in photodynamic therapy (PDT), diagnostic arrays and water treatments.[34,35] With this purpose, Pc have also been incorporated in the inner cavity of virus capsids as delivery vehicles.[36−38] However, Pc derivatives tend to stack in aqueous conditions,[39] deactivating the excited state and thus limit their scope of application. Furthermore, Pc systems are challenging to be organized in crystalline phases.

RESULTS

In order to tackle these challenges, we decided to study an octacationic ZnPc with eight quaternized pyridyloxy peripheral substituents (**1**), which is highly water-soluble and can bind to the negative domains on the exterior surface of **aFt** (Figure 1). As for most Pcs, the UV−vis spectrum of **1** in phosphate buffered saline (PBS) solution, containing 187 mM NaCl to mimic physiological conditions, reveals the formation of aggregates. This can be observed as the broadness and strong splitting of the ZnPc Q-band to a higher frequency, with an intense absorption at 635 nm that is characteristic of hypsochromic H-type aggregation (Figure S1, blue curve).[40] We then probed the noncovalent complexation of ZnPc **1** with tetraanionic PTSA (**2**) in the same buffer conditions, rationalizing that in a 1:1 stoichiometry the complex would still leave 4 positive charges for further binding to **aFt**. Interestingly, the addition of **2** to **1**, up to a 1:1 molar ratio, increased the Q-band intensity and shifted its maximum from 669 to 680 nm, while no absorption peak due to the ZnPc H-type aggregates at 635 nm was remaining (Figure 2a and S1).

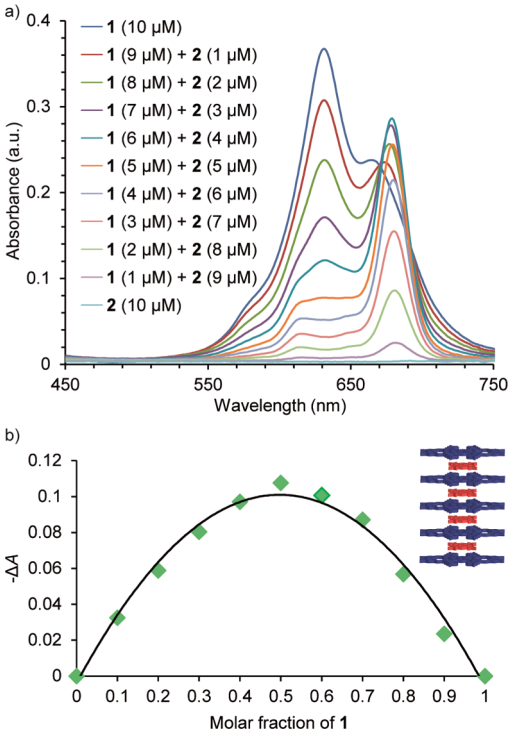

Figure 2. (a) UV−Vis spectra of 1−2 complexes with molar ratios ranging from 10:0 to 0:10 and fixed overall concentration of both components (10 μM). (b) Job plot diagram derived from measurements presented in (a) confirms that 1 and 2 self-assemble into a complex with a stoichiometric 1:1 ratio schematically depicted in the inset.

DOI: 10.1021/acsnano.5b07167
ACS Nano 2016, 10, 1565−1571

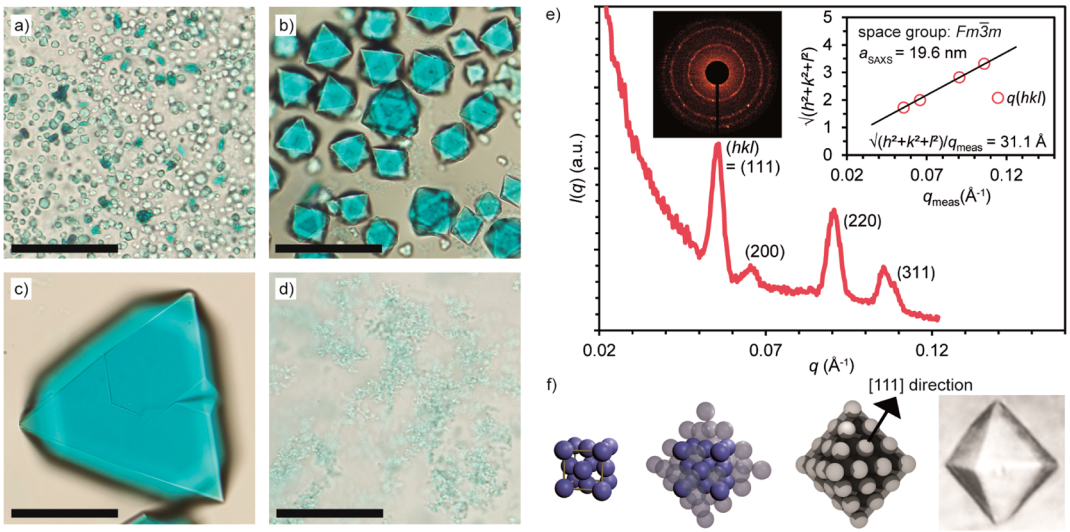

Figure 3. 1−2−aFt crystals self-assembled in (a) 0 mM, (b) 20 mM, (c) 30 mM, (d) 40 mM NaCl solutions. Scale bars in all images are 50 μm. (e) SAXS data from 1−2−aFt crystals in 20 mM NaCl concentration indicates an fcc crystal structure for the 1−2−aFt crystals. Top left inset shows the 2D scattering pattern and top right inset shows the Quadratic Miller indices of assigned reflections for *Fm*$\bar{3}$*m* structure *versus* measured *q*-vector positions. Solid line presents a linear fit, which yields the lattice constant a_{SAXS} and the aFt center-to-center distance d_{cc}. All samples were prepared in 5 mM tris buffer (pH 8.5). (f) Schematic presentation of the suggested 1−2−aFt crystal formation (left) and regular octahedron shape observed in optical microscopy (right).

Further additions of **2** caused only minor changes in the absorption spectra. These results were taken as an indication of ZnPc-PTSA complexation. The 1:1 stoichiometry of the complex was confirmed with the Job plot method performed by measuring the UV−vis spectra of samples containing different mole fractions of **1** and **2** (Figure 2b and S2). Absorption titration (Figure S3) was conducted, which allowed determining an association constant of $1.73 \pm 0.03 \times 10^6$ M^{-1}. Furthermore, fluorescence titration (Figure S5) showed a significant recovery of the ZnPc emission upon complexation, supporting that self-quenching of the excited state is not taking place in the complex. Overall, these studies proved the strong binding between **1** and **2**, even in relatively high electrolyte concentration, and the concomitant recovery of the pristine ZnPc photochemical properties (see below), otherwise lost in PBS solution.

Next we studied the crystal formation from **1−2** complexes and **aFt** from *Pyrococcus furiosus*. We chose spherical and hollow **aFt**, because it can be used to store for example small molecules or noble metal nanoparticles inside the 8 nm sized inner cavity, and therefore, it offers a flexible platform for designing multifunctional protein complexes.[28,41−44] The outer diameter of **aFt** is 12 nm and the cage consists of 24 protein subunits (Figure 1b). We thus combined and mixed **1**, **2**, as well as **aFt** in a buffer solution containing 5 mM Tris (pH 8.5) and 0−200 mM NaCl to tune the electrostatic interactions. Samples were left overnight into a fridge (+7 °C) resulting in ternary **1−2−aFt** crystals. The stoichiometric ratio of **1**/**2**/**aFt** in the sample solutions was 100:100:1.

The crystals were first studied with optical microscopy (Figure 3a−d). In the samples with 0 mM NaCl mostly poorly defined amorphous complexes were assembled, but in 30 mM NaCl concentration large, up to 100 μm sized, **1−2−aFt** crystals were observed. The crystals have clearly visible faceting and overall uniform octahedral crystal habit. Increasing the electrolyte concentration shortens the distance over which charged particles interact electrostatically with each other (Debye screening length). The higher electrolyte concentration reduces the strength of the binding and therefore helps to avoid kinetically trapped structures and promotes the formation of larger crystal domains, which can be considered as the thermodynamic product. However, when the electrolyte concentration is further increased, the Debye screening length is decreased remarkably and as a result the electrostatic attraction between the components are efficiently screened.[14,17,19,21] Also in the case of our samples prepared with 40 mM or higher NaCl concentration, no distinct assemblies were present, which implies that at these conditions the electrostatic interactions between **1−2** complexes and **aFt** are strongly interfered. Increasing the NaCl concentration to 100 mM in samples with preformed large crystals rapidly disassembled them (Figure S7). We also found that the crystals could be removed from the solvent and dried to yield free-standing crystals. As a reference, we prepared samples where only **1** and **aFt** were combined, without **2** (Figure S6). In general, the samples behaved in a similar manner, although the observed crystals were less defined at 40 mM or higher NaCl concentration.

The **1−2−aFt** crystals were studied further by small-angle X-ray scattering (SAXS) (Figure 3e), in order to characterize the crystal symmetry and lattice spacing. The SAXS data for crystals formed in 20 mM NaCl concentration is dominated by intensive diffraction peaks, which fit to a face-centered cubic (fcc) crystal structure. The four first diffraction peaks ((hkl) = (111), (200), (220), (311); q:q^* = 1, $\sqrt{(4/3)}$, $\sqrt{(8/3)}$, $\sqrt{(11/3)}$) of the fcc structure (space group *Fm*$\bar{3}$*m*; number 225) are unambiguously identified at q = (0.056, 0.065, 0.091, 0.105) $Å^{-1}$. It is known that **aFt** protein cages alone tend to form an fcc structure (a = 18.3−18.5 nm) upon crystallization[45−47] and that the crystallization proceeds by growing fastest in the direction of the hexagonally patterned {111} planes,[48,49] giving rise to an octahedral crystal habit. We postulate that the crystal growth in our system proceeds in analogous manner to yield the observed regular octahedron shape of the crystals (Figure 3f). Measured lattice constant a_{SAXS} was 19.6 nm (for cubic phases $a = 2\pi\sqrt{(h^2 + k^2 + l^2)}/q_{(hkl)}$) and the center-to-center

DOI: 10.1021/acsnano.5b07167
ACS Nano 2016, 10, 1565−1571

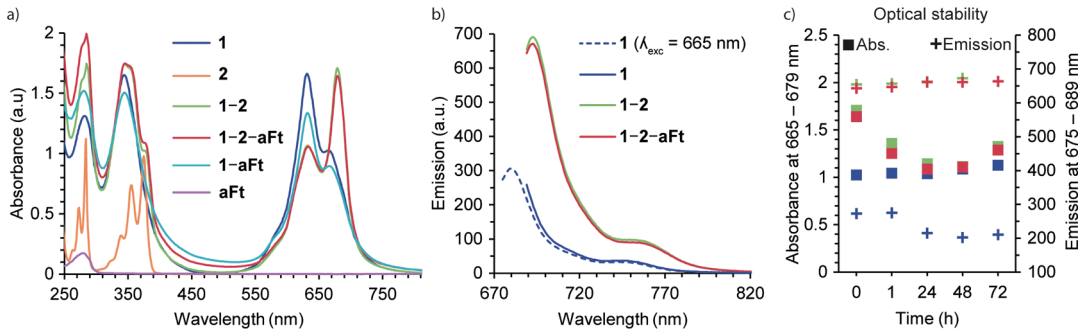

Figure 4. (a) Absorption spectrum of 1−2−aFt crystals self-assembled in 30 mM NaCl (5 mM Tris buffer, pH 8.5) and the reference samples. (b) Fluorescence emission of 1 (λ_{exc} = 665 and 679 nm), 1−2 and the 1−2−aFt crystals (λ_{exc} = 679 nm), with excitation wavelengths adjusted according to the corresponding excitation spectra. (c) Absorbance and fluorescence of 1−2−aFt (red symbols) and reference samples (1, blue symbols; 1−2, green symbols) measured over time. Left *y*-axis shows the absorbance at the absorption maxima at 665 nm (1) or at 679 nm (1−2 and 1−2−aFt). Right *y*-axis shows the fluorescence intensity at 675 nm (1, λ_{exc} = 665) or at 689 nm (1−2 and 1−2−aFt, λ_{exc} = 679).

distance d_{cc} between **aFt** units was 13.8 nm. The d_{cc} corresponds well to the dimensions of **aFt** (12 nm) coated with **1−2** complexes.

In order to probe the potential applicability of the presented biohybrid crystals, we studied whether the crystal formation with **aFt** affects the optical properties of the **1−2** complex. The absorption spectrum of the ternary assemblies, in the presence of 30 mM NaCl concentration, was measured (Figure 4a). By comparison to the reference samples, *i.e.*, **1**, **2**, and **1−2** in the same conditions as for the **1−2−aFt** crystals, we could infer that the binding between **1** and **2** is not broken in the crystalline structure, having similar absorption features for the **1−2** complex (Figure 4a). As an additional control, the spectrum of **1** combined with only **aFt** was also recorded, showing that the protein cage in absence of **2** is not able to break the ZnPc aggregates.

A similar experiment was conducted utilizing fluorescence spectroscopy (Figure 4b). Excitation took place at the wavelength that maximizes emission, *i.e.*, at 665 nm for **1** and at 679 nm for **1−2** and the **1−2−aFt** crystals, according to the corresponding excitation spectra. A solution of **1** was excited also at 679 nm to make the comparison of the samples more profound. The concentration of the ZnPc in all samples was adjusted to 5 μM by dilution. Interestingly, the emission profile of the **1−2** and **1−2−aFt** samples had a similar shape and their intensities more than doubled that of **1** alone, when exciting with the given wavelengths. Again, this result indicates that crystallization does not alter the optical properties of the **1−2** complex. The remarkable fluorescence properties of the crystals at the NIR spectral region may be of utility in biomedical technologies that involve an optical imaging step. Finally, Figure 4c shows that all samples were stable over time, as no major changes occurred in their absorption or fluorescence after the complexes had formed.

Considering the multiple applications that photoinduced $^1O_2$ presents (see above), showing the functional photosensitizing properties of the biohybrid crystals is critically important. The $^1O_2$ quantum yield (Φ_Δ) of **1** was determined in DMSO using the *relative method*,[50] based on measuring the rate of photodegradation of a chemical scavenger (1,3-diphenylisobenzofuran, DPBF) that is directly proportional to the formation of $^1O_2$ (see SI for further details). DMSO, as a coordinating solvent, disrupts the aggregation of **1** by coordination to the zinc metal center, resulting in a Φ_Δ value of 0.72 (nonsubstituted ZnPc was taken as reference: $\Phi_{\Delta(DMSO)}$ = 0.67), which indicates the excellent photosensitizing ability of **1** when it does not self-quench its excited state.

For measuring complex **1−2** and the **1−2−aFt** crystals, in turn, aqueous solubility of the scavenger was required. DPBF was then dispersed, from a concentrated solution in DMSO (c.a. 1 mM), into a solution of the common neutral pharmaceutical solubilizer Cremophor EL (0.5% w/w) in the 5 mM Tris buffer, together with the corresponding photosensitizing system (*i.e.*, **1**, **1−2** or **1−2−aFt**). The absorbance of all samples at the Q-band maximum wavelength was adjusted to 0.1, to ensure that the concentration of PS was approximately equal in all samples. Figure S10 shows an example of the decay of the scavenger absorption during these experiments. A decrease in Q-band intensity, or appearance of new bands were not observed in any case, confirming the integrity of the photosensitizing system throughout the whole experiment. Under these circumstances, plotting the dependence of $\ln(A_0/A_t)$ against irradiation time (t) (with A_0 and A_t being the respective scavenger absorbance values at the monitoring wavelength before and after the irradiation time t) affords a straight line whose slope reflects the PS efficacy to generate $^1O_2$. Figure 5a then represents the scavenger photodegradation profiles induced by all samples under study and a nonsubstituted ZnPc used as reference compound. A dark control was performed, showing that none of the samples induced DPBF bleaching in the absence of irradiation. Importantly, the **1−2** complex photogenerates $^1O_2$ almost as efficiently as **1**, especially when it is cocrystallized with **aFt**. We can consequently conclude that **1−2−aFt** represents the very first case of a highly efficient photosensitizing crystalline structure.

Finally, we also studied if irradiation of the **1−2−aFt** crystals causes photodamage to **aFt** (Figures 5b and S11). This was carried out by irradiating them over different periods of time, long enough to entirely bleach the scavenger. The experiment was monitored by UV−Vis spectroscopy and SDS-PAGE after each irradiation period (for more details see the SI). Overall, no degradation of **aFt** was observed, indicating that the protein cage is resistant to $^1O_2$ and therefore the present crystalline platform is a sufficiently robust PS system for practical applications.

CONCLUSIONS

In summary, we have developed a hierarchical protocol to organize organic dyes and protein cages into functional ternary superlattices. The self-assembly of our quantized nanoscale

DOI: 10.1021/acsnano.5b07167
ACS Nano 2016, 10, 1565−1571

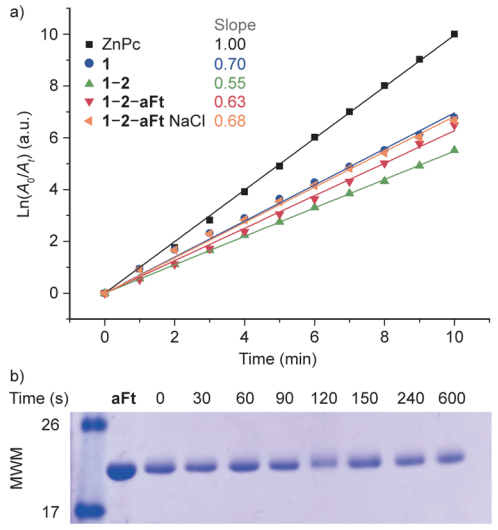

Figure 5. (a) Normalized absorption ($\ln(A_0/A_t)$) of DPBF over time, showing its photodegradation rate in the presence of different PS systems. Solid lines present linear fits from which the slope is directly proportional to the photoinduced generation of $^1O_2$. ZnPc accounts for the nonsubstituted derivative used as reference compound. (b) 1−2−aFt crystal dispersion irradiated for different times and analyzed by SDS-PAGE. Molecular weight markers (MWM) are given on the left (kDa).

building blocks into stoichiometric higher order structures can also be regarded as an example of nanoscale atom mimicry.[51,52] Our strategy is based on the formation of a supramolecular complex between octacationic ZnPc and tetraanionic pyrene derivatives, driven by electrostatic and $\pi-\pi$ interactions, which in turn binds to the negatively charged patches in the **aFt** protein cage exterior surface, acting as a molecular glue that induces cocrystallization. The resulting crystals are photoactive and robust biohybrid materials that emit fluorescence and can generate highly reactive $^1O_2$ without self-degradation upon irradiation. Moreover, such fcc-packed crystals, with diameters up to 100 μm, can be disassembled by increasing the electrolyte concentration. We envision that this kind of functional, highly ordered systems could be utilized, for example, to develop recyclable and environmentally benign water treatment agents, diagnostic arrays or photocatalytic crystals (*e.g.*, for oxidation processes). Furthermore, the supramolecular approach is fully modular and can be easily extended to other cationic organic dyes that present different optoelectronic properties or **aFt** loaded with functional materials.

MATERIALS AND METHODS

Materials. Octakis(1-methyl-3-pyridiniumoxy)-ZnPc tetrasulfate (**1**) was synthesized as reported earlier.[27] All other reagents, including 1,3,6,8-pyrenetetrasulfonic acid tetrasodium, salt hydrate (**2**) were commercially available and used without any further purification. The water used in all procedures was Milli-Q purified. Stock solutions of **1** and **2** were prepared by diluting chemicals in pure water, phosphate-buffered saline (PBS buffer, 10 mM Na_2HPO_4, 2.7 mM KCl, 187 mM NaCl, pH 7.4) or Tris buffer (20 mM Tris, pH 8.5). Apoferritin (**aFt**) from *Pyrococcus furiosus* was ordered from Molirom and it was delivered as a 10 mg/mL water solution.

UV−Vis Spectroscopy. UV−vis spectroscopy of **1**, **2** and the **1−2** complex in PBS buffer were recorded using a JASCO V-660 spectrophotometer. Sample solutions (2.4−3 mL) were measured at room temperature using a Hellma QS quartz cuvette with 1 cm light path. Absorbance between 250 and 850 nm was scanned with 1 nm resolution. The UV−vis spectra of the **1−2−aFt** crystals in Tris buffer were recorded using a Biotek Cytation 3 Imaging reader and a Take3 microvolume plate. Absorbance of 3 μL sample volumes were scanned between 230 and 900 nm with 1 nm increments at room temperature.

Fluorescence Spectroscopy. The fluorescence spectra of **1**, **2** and the **1−2** complex in PBS buffer were recorded using a JACSO FP-8600 fluorescence spectrophotometer at room temperature. Samples were excited in a 3.5 mL Hellma QS quartz fluorescence cell, with 669−681 nm excitation wavelength depending on the maximum observed in the excitation spectra measured in advance. Emission was recorded from a 10 nm higher wavelength than the exciting wavelength until 850 nm in 1 nm steps. The fluorescence spectra of the **1−2−aFt** crystals in Tris buffer and after washing the crystals were recorded on a Cary Eclipse fluorescence spectrophotometer (Agilent Technologies) at room temperature. Samples were diluted to a 2 mL volume and measured in disposable PMMA cuvettes (Brand) with four clear faces. Samples were excited, with 665−679 nm wavelength depending on the maximum observed in the excitation spectra measured in advance. Emission was recorded from a 10 nm higher wavelength than the exciting wavelength until 900 nm in 1 nm steps.

Optical Microscopy. Sample solutions of 20 μL were placed on a marienfeld-superior microscope slide (76 × 26 × 1.35 mm with a round cavity of 15−18 mm diameter and 0.6−0.8 mm depth) and a cover glass was placed on the sample. Samples were imaged with Leica DM4500 P optical microscope equipped with Canon EOS 60D camera using transmission mode. A ruler at the sample position was imaged to calibrate the scale of the images.

Small Angle X-ray Scattering. Small-angle X-ray scattering measurements were carried out using a rotating anode Bruker Microstar microfocus X-ray source (Cu Kα radiation, λ = 1.54 Å). The X-ray beam was monochromated and focused by a Montel multilayer focusing monochromator (Incoatec). The beam was further collimated by four slits (JJ X-ray) resulting in a beam size of less than 1 mm at the sample position. The scattering was collected using Hi-Star 2D area detector (Bruker). The used sample-to-detector distance was 1.59 m, and silver behenate standard sample was used to calibrate the q-range. One-dimensional SAXS data were obtained by azimuthally averaging the 2D scattering data. The magnitude of the scattering vector q is given by $q = 4\pi \sin\theta/\lambda$, where 2θ is the scattering angle. The samples were measured without pretreatment, for example 10 μL of **1−2−aFt** crystal sample solution was sealed in a metal ring using Kapton tape. Sample thickness was approximately 0.9 mm. The sample environment was evacuated during the measurements to avoid scattering from air.

Singlet Oxygen Generation. The singlet oxygen ($^1O_2$) quantum yield (Φ_Δ) of ZnPc **1** was first measured in DMSO following the well-known *relative method*, based on the photoinduced decomposition of a chemical scavenger (*i.e.*, 1,3-diphenylisobenzofuran (DPBF) that reacts readily with $^1O_2$. Nonsubstituted ZnPc was used as reference compound ($\Phi_{\Delta(DMSO)} = 0.67$). In detail, the procedure was as follows: 2.5 mL of a stock solution of DPBF (with an absorbance of *ca.* 1) in DMSO was transferred into a 1 × 1 cm quartz optical cell and bubbled with oxygen for 1 min. A concentrated stock solution of the Pc in the same solvent was then added, in a defined amount to reach a final Q-band absorbance value of about 0.1. The solution was stirred and irradiated for defined time intervals, using a halogen lamp (typically, 300 W). The duration of these intervals are tuned in each experiment, in order to get a decrease in DPBF absorption of about 3−4%. Incident light was filtered through a water filter (6 cm) and an additional filter to remove light under 530 nm (Newport filter FSQ-OG530). The decrease of DPBF concentration with irradiation time was monitored at 414 nm using a JASCO V-660 spectrophotometer and a Hellma QS quartz fluorescence cell with 1 cm light path. All experiments were performed three times and the obtained data represent mean values of those three experiments. The estimated error is ±10%.

SDS-PAGE. Fractions containing irradiated **1−2−aFt** crystals for different times (30 s−6 min) were added to Laemmli simple buffer to a 1x final concentration (62.5 mM Tris−HCl, 2% SDS, 5% glycerol, 0.012% bromophenol blue, 2 mM dithiothreitol, pH 6.8), heated (3

DOI: 10.1021/acsnano.5b07167
ACS Nano 2016, 10, 1565−1571

min, 100 °C), and resolved in 14% polyacrylamide gels at 20 °C until the dye reached the gel bottom. Samples were visualized by Coomassie blue staining.

ASSOCIATED CONTENT

Supporting Information

The Supporting Information is available free of charge on the ACS Publications website at DOI: 10.1021/acsnano.5b07167.

Details of materials and sample preparations. Experimental details and additional results from UV−vis spectroscopy, fluorescence spectroscopy, **1**−**2** complexation studies, optical microscopy, small-angle X-ray scattering, transmission electron microscopy, $^1O_2$ generation studies and evaluation of protein photodamage. (PDF)

AUTHOR INFORMATION

Corresponding Authors

*E-mail: tomas.torres@uam.es.
*E-mail: andres.delaescosura@uam.es.
*E-mail: mauri.kostiainen@aalto.fi.

Notes

The authors declare no competing financial interest.

ACKNOWLEDGMENTS

J.M., V.L. and M.A.K. acknowledge support through the Emil Aaltonen Foundation and the Academy of Finland (grants 267497, 273645 and 263504). AdlE acknowledges a Ramón y Cajal contract from the Spanish Ministry of Economy (MINECO). This work was supported by the Academy of Finland through its Centres of Excellence Programme (2014-2019). This work made use of the Aalto University Nanomicroscopy Centre (Aalto NMC). The work at Madrid was supported by the EU (GLOBASOL, FP7-ENERGY-2012-J, 309194-2 and SO2S, FP7-PEOPLE-2012-ITN, 316975), the Spanish MINECO (BFU2014-55475R (JRC), CTQ-2014-52869-P (TT) and CTQ-2014-53673-P (AdlE)) and Comunidad de Madrid (S2013/MIT-2807 (JRC), FOTOCARBON, S2013/MIT-2841 (TT)).

REFERENCES

(1) Macfarlane, R. J.; Jones, M. R.; Lee, B.; Auyeung, E.; Mirkin, C. A. Topotactic Interconversion of Nanoparticle Superlattices. *Science* **2013**, *341*, 1222−1225.

(2) Chung, W.-J.; Oh, J.-W.; Kwak, K.; Lee, B. Y.; Meyer, J.; Wang, E.; Hexemer, A.; Lee, S.-W. Biomimetic Self-Templating Supramolecular Structures. *Nature* **2011**, *478*, 364−368.

(3) de Nijs, B.; Dussi, S.; Smallenburg, F.; Meeldijk, J. D.; Groenendijk, D. J.; Filion, L.; Imhof, A.; van Blaaderen, A.; Dijkstra, M. Entropy-Driven Formation of Large Icosahedral Colloidal Clusters by Spherical Confinement. *Nat. Mater.* **2015**, *14*, 56−60.

(4) Ruiz-Hitzky, E.; Darder, M.; Aranda, P.; Ariga, K. Advances in Biomimetic and Nanostructured Biohybrid Materials. *Adv. Mater.* **2010**, *22*, 323−336.

(5) Lee, S.-Y.; Lim, J.-S.; Harris, M. T. Synthesis and Application of Virus-Based Hybrid Nanomaterials. *Biotechnol. Bioeng.* **2012**, *109*, 16−30.

(6) Abe, S.; Ueno, T. Design of Protein Crystals in the Development of Solid Biomaterials. *RSC Adv.* **2015**, *5*, 21366−21375.

(7) Auyeung, E.; Morris, W.; Mondloch, J. E.; Hupp, J. T.; Farha, O. K.; Mirkin, C. A. Controlling Structure and Porosity in Catalytic Nanoparticle Superlattices with DNA. *J. Am. Chem. Soc.* **2015**, *137*, 1658−1662.

(8) Brodin, J. D.; Auyeung, E.; Mirkin, C. A. DNA-Mediated Engineering of Multicomponent Enzyme Crystals. *Proc. Natl. Acad. Sci. U. S. A.* **2015**, *112*, 4564−4569.

(9) Royston, E.; Ghosh, A.; Kofinas, P.; Harris, M. T.; Culver, J. N. Self-Assembly of Virus-Structured High Surface Area Nanomaterials and Their Application as Battery Electrodes. *Langmuir* **2008**, *24*, 906−912.

(10) Lee, S.-W.; Mao, C.; Flynn, C. E.; Belcher, A. M. Ordering of Quantum Dots Using Genetically Engineered Viruses. *Science* **2002**, *296*, 892−895.

(11) Slocik, J. M.; Tam, F.; Halas, N. J.; Naik, R. R. Peptide-Assembled Optically Responsive Nanoparticle Complexes. *Nano Lett.* **2007**, *7*, 1054−1058.

(12) Sakai, F.; Yang, G.; Weiss, M. S.; Liu, Y.; Chen, G.; Jiang, M. Protein Crystalline Frameworks with Controllable Interpenetration Directed by Dual Supramolecular Interactions. *Nat. Commun.* **2014**, *5*, 4634.

(13) Chen, C.-F.; Tzeng, S.-D.; Chen, H.-Y.; Lin, K.-J.; Gwo, S. Tunable Plasmonic Response from Alkanethiolate-Stabilized Gold Nanoparticle Superlattices: Evidence of near-Field Coupling. *J. Am. Chem. Soc.* **2008**, *130*, 824−826.

(14) Kostiainen, M. A.; Hiekkataipale, P.; Laiho, A.; Lemieux, V.; Seitsonen, J.; Ruokolainen, J.; Ceci, P. Electrostatic Assembly of Binary Nanoparticle Superlattices Using Protein Cages. *Nat. Nanotechnol.* **2013**, *8*, 52−56.

(15) Paik, T.; Diroll, B. T.; Kagan, C. R.; Murray, C. B. Binary and Ternary Superlattices Self-Assembled from Colloidal Nanodisks and Nanorods. *J. Am. Chem. Soc.* **2015**, *137*, 6662−6669.

(16) O'Brien, M. N.; Jones, M. R.; Lee, B.; Mirkin, C. A. Anisotropic Nanoparticle Complementarity in DNA-Mediated Co-Crystallization. *Nat. Mater.* **2015**, *14*, 833−839.

(17) Liljeström, V.; Mikkilä, J.; Kostiainen, M. A. Self-Assembly and Modular Functionalization of Three-Dimensional Crystals from Oppositely Charged Proteins. *Nat. Commun.* **2014**, *5*, 4445.

(18) Uchida, M.; LaFrance, B.; Broomell, C. C.; Prevelige, P. E.; Douglas, T. Higher Order Assembly of Virus-like Particles (VLPs) Mediated by Multi-Valent Protein Linkers. *Small* **2015**, *11*, 1562−1570.

(19) Mikkilä, J.; Rosilo, H.; Nummelin, S.; Seitsonen, J.; Ruokolainen, J.; Kostiainen, M. A. Janus-Dendrimer-Mediated Formation of Crystalline Virus Assemblies. *ACS Macro Lett.* **2013**, *2*, 720−724.

(20) Välimäki, S.; Mikkilä, J.; Liljeström, V.; Rosilo, H.; Ora, A.; Kostiainen, M. A. Hierarchically Ordered Supramolecular Protein-Polymer Composites with Thermoresponsive Properties. *Int. J. Mol. Sci.* **2015**, *16*, 10201−10213.

(21) Liljeström, V.; Seitsonen, J.; Kostiainen, M. A. Electrostatic Self-Assembly of Soft Matter Nanoparticle Cocrystals with Tunable Lattice Parameters. *ACS Nano* **2015**, *9*, 11278−11285.

(22) Jutz, G.; van Rijn, P.; Santos Miranda, B.; Böker, A. Ferritin: A Versatile Building Block for Bionanotechnology. *Chem. Rev.* **2015**, *115*, 1653−1701.

(23) de la Escosura, A.; Nolte, R. J. M.; Cornelissen, J. J. L. M. Viruses and Protein Cages as Nanocontainers and Nanoreactors. *J. Mater. Chem.* **2009**, *19*, 2274−2278.

(24) Yoo, J.-W.; Irvine, D. J.; Discher, D. E.; Mitragotri, S. Bio-Inspired, Bioengineered and Biomimetic Drug Delivery Carriers. *Nat. Rev. Drug Discovery* **2011**, *10*, 521−535.

(25) Ma, Y.; Nolte, R. J. M.; Cornelissen, J. J. L. M. Virus-Based Nanocarriers for Drug Delivery. *Adv. Drug Delivery Rev.* **2012**, *64*, 811−825.

(26) Zeng, Q.; Wen, H.; Wen, Q.; Chen, X.; Wang, Y.; Xuan, W.; Liang, J.; Wan, S. Cucumber Mosaic Virus as Drug Delivery Vehicle for Doxorubicin. *Biomaterials* **2013**, *34*, 4632−4642.

(27) Li, H.; Jensen, T. J.; Fronczek, F. R.; Vicente, M. G. H. Syntheses and Properties of a Series of Cationic Water-Soluble Phthalocyanines. *J. Med. Chem.* **2008**, *51*, 502−511.

DOI: 10.1021/acsnano.5b07167
ACS Nano 2016, 10, 1565−1571

(28) Tatur, J.; Hagen, W. R.; Matias, P. M. Crystal Structure of the Ferritin from the Hyperthermophilic Archaeal Anaerobe Pyrococcus Furiosus. *JBIC, J. Biol. Inorg. Chem.* **2007**, *12*, 615−630.
(29) Kadish, K. M.; Smith, K. M.; Guilard, R. *Handbook of Porphyrin Science*; World Scientific, 2013.
(30) Roznyatovskiy, V. V.; Lee, C.-H.; Sessler, J. L. π-Extended Isomeric and Expanded Porphyrins. *Chem. Soc. Rev.* **2013**, *42*, 1921−1933.
(31) de la Torre, G.; Claessens, C. G.; Torres, T. Phthalocyanines: Old Dyes, New Materials. Putting Color in Nanotechnology. *Chem. Commun.* **2007**, 2000−2015.
(32) Bezzu, C. G.; Helliwell, M.; Warren, J. E.; Allan, D. R.; McKeown, N. B. Heme-like Coordination Chemistry within Nanoporous Molecular Crystals. *Science* **2010**, *327*, 1627−1630.
(33) Mack, J.; Kobayashi, N. Low Symmetry Phthalocyanines and Their Analogues. *Chem. Rev.* **2011**, *111*, 281−321.
(34) DeRosa, M. C.; Crutchley, R. J. Photosensitized Singlet Oxygen and Its Applications. *Coord. Chem. Rev.* **2002**, *233−234*, 351−371.
(35) Ashen-Garry, D.; Selke, M. Singlet Oxygen Generation by Cyclometalated Complexes and Applications. *Photochem. Photobiol.* **2014**, *90*, 257−274.
(36) Brasch, M.; de la Escosura, A.; Ma, Y.; Uetrecht, C.; Heck, A. J. R.; Torres, T.; Cornelissen, J. J. L. M. Encapsulation of Phthalocyanine Supramolecular Stacks into Virus-like Particles. *J. Am. Chem. Soc.* **2011**, *133*, 6878−6881.
(37) Luque, D.; de la Escosura, A.; Snijder, J.; Brasch, M.; Burnley, R. J.; Koay, M. S. T.; Carrascosa, J. L.; Wuite, G. J. L.; Roos, W. H.; Heck, A. J. R.; et al.*et al.* Self-Assembly and Characterization of Small and Monodisperse Dye Nanospheres in a Protein Cage. *Chem. Sci.* **2014**, *5*, 575−581.
(38) Setaro, F.; Brasch, M.; Hahn, U.; Koay, M. S. T.; Cornelissen, J. J. L. M.; de la Escosura, A.; Torres, T. Generation-Dependent Templated Self-Assembly of Biohybrid Protein Nanoparticles around Photosensitizer Dendrimers. *Nano Lett.* **2015**, *15*, 1245−1251.
(39) Dumoulin, F.; Durmuş, M.; Ahsen, V.; Nyokong, T. Synthetic Pathways to Water-Soluble Phthalocyanines and Close Analogs. *Coord. Chem. Rev.* **2010**, *254*, 2792−2847.
(40) Nyokong, T. Effects of Substituents on the Photochemical and Photophysical Properties of Main Group Metal Phthalocyanines. *Coord. Chem. Rev.* **2007**, *251*, 1707−1722.
(41) Chasteen, N. D.; Harrison, P. M. Mineralization in Ferritin: An Efficient Means of Iron Storage. *J. Struct. Biol.* **1999**, *126*, 182−194.
(42) Zhen, Z.; Tang, W.; Chen, H.; Lin, X.; Todd, T.; Wang, G.; Cowger, T.; Chen, X.; Xie, J. RGD-Modified Apoferritin Nanoparticles for Efficient Drug Delivery to Tumors. *ACS Nano* **2013**, *7*, 4830−4837.
(43) Kasyutich, O.; Ilari, A.; Fiorillo, A.; Tatchev, D.; Hoell, A.; Ceci, P. Silver Ion Incorporation and Nanoparticle Formation inside the Cavity of Pyrococcus Furiosus Ferritin: Structural and Size-Distribution Analyses. *J. Am. Chem. Soc.* **2010**, *132*, 3621−3627.
(44) Kim, M.; Rho, Y.; Jin, K. S.; Ahn, B.; Jung, S.; Kim, H.; Ree, M. pH-Dependent Structures of Ferritin and Apoferritin in Solution: Disassembly and Reassembly. *Biomacromolecules* **2011**, *12*, 1629−1640.
(45) Hempstead, P. D.; Yewdall, S. J.; Fernie, A. R.; Lawson, D. M.; Artymiuk, P. J.; Rice, D. W.; Ford, G. C.; Harrison, P. M. Comparison of the Three-Dimensional Structures of Recombinant Human H and Horse L Ferritins at High Resolution. *J. Mol. Biol.* **1997**, *268*, 424−448.
(46) Lawson, D. M.; Artymiuk, P. J.; Yewdall, S. J.; Smith, J. M. A.; Livingstone, J. C.; Treffry, A.; Luzzago, A.; Levi, S.; Arosio, P.; Cesareni, G.; et al.*et al.* Solving the Structure of Human H Ferritin by Genetically Engineering Intermolecular Crystal Contacts. *Nature* **1991**, *349*, 541−544.
(47) Thomas, B.; Carter, D.; Rosenberger, F. Effect of Micro-heterogeneity on Horse Spleen Apoferritin Crystallization. *J. Cryst. Growth* **1998**, *187*, 499−510.
(48) Yau, S.-T.; Vekilov, P. G. Quasi-Planar Nucleus Structure in Apoferritin Crystallization. *Nature* **2000**, *406*, 494−497.
(49) Yau, S.-T.; Vekilov, P. G. Direct Observation of Nucleus Structure and Nucleation Pathways in Apoferritin Crystallization. *J. Am. Chem. Soc.* **2001**, *123*, 1080−1089.
(50) Nombona, N.; Maduray, K.; Antunes, E.; Karsten, A.; Nyokong, T. Synthesis of Phthalocyanine Conjugates with Gold Nanoparticles and Liposomes for Photodynamic Therapy. *J. Photochem. Photobiol., B* **2012**, *107*, 35−44.
(51) Tomalia, D. A. Dendrons/dendrimers: Quantized, Nano-Element like Building Blocks for Soft-Soft and Soft-Hard Nano-Compound Synthesis. *Soft Matter* **2010**, *6*, 456−474.
(52) Tomalia, D. A.; Khanna, S. N. In Quest of a Systematic Framework for Unifying and Defining Nanoscience. *Mod. Phys. Lett. B* **2014**, *28*, 1430002.

DOI: 10.1021/acsnano.5b07167
ACS Nano 2016, 10, 1565−1571